

We are IntechOpen, the world's leading publisher of Open Access books Built by scientists, for scientists

6,900

Open access books available

185,000

International authors and editors

200M

Downloads

Our authors are among the

154

Countries delivered to

TOP 1%

most cited scientists

12.2%

Contributors from top 500 universities



WEB OF SCIENCE™

Selection of our books indexed in the Book Citation Index
in Web of Science™ Core Collection (BKCI)

Interested in publishing with us?
Contact book.department@intechopen.com

Numbers displayed above are based on latest data collected.
For more information visit www.intechopen.com



Graphene Acoustic Devices

*He Tian, Guang-Yang Gou, Fan Wu, Lu-Qi Tao, Yi Yang
and Tian-Ling Ren*

Abstract

In 2011, Ren's group has developed the first graphene sound source device in the world. This is the first time that the graphene applications have been extended into acoustic area. The graphene sound source can produce sound in a wide sound frequency range from 100 Hz to 50 kHz. After that, we have innovated the first graphene earphone, which can be used both for human and animals. In 2017, both the sound detection and sound emission have been integrated into one graphene device, which is called graphene artificial throat. In this book chapter, more details for developing those graphene acoustic devices will be introduced, which can help to boost the real applications of graphene devices.

Keywords: graphene sound, acoustic, thermoacoustic effect, wide frequency range, flexible, large-scale

1. Introduction

Since graphene have been found in 2004 [1], various kinds of graphene-based devices, including field effect transistor (FET) [2], memory [3], photodetector [4], sensor [5], have been built as its excellent structural and physical properties. However, almost no work was focused on the acoustic device in audio range because the graphene is hard to make low frequency sound through vibration due to the large-area requirement. Although the working principles of traditional sound devices are different, they are all depend on mechanical vibration of thin films, and driving the air to produce the sound. There is a common problem that the output audio spectrum of these sound devices is not flat, which is caused by the inherent center resonance of the diaphragm. Here, thermoacoustic effect is proposed to emit sound without vibration of the diagram. The conductive film itself can emit sound, which will be expected to achieve wide-band acoustic output. In 1917, Arnold's group firstly used the 700 nm-Pt film as the source to realize thermoacoustic sound production [6]. The sound frequency of this device can reach to 40 kHz, but the sound pressure (SP) was not high enough. With the rapid development of nanotechnology in recent years, many outstanding progresses have been made in sound source devices based on thermoacoustic effect. In 1999, Shinoda's group have reported aluminum thin film sound device based on porous silicon substrate, and the wide output band can be implemented in 20–100 kHz [7]. Especially, the SP of the device is up to 0.1 Pa. After that, the research group in Tsinghua University realized the sound source device based on carbon nanotubes [8]. This thermoacoustic device not only can produce high sound pressure level (SPL) in a wide audio range, but also have the advantages of bending, stretching and transparency.

However, most of thermoacoustic devices have some problems and technical limitations in material preparation, device structure and working mechanism. For example, the performance of aluminum thin film thermoacoustic device is seriously degraded because the aluminum is easily oxidized in air, and the device is rigid and non-transparent [7]. For the thermoacoustic device based on carbon nanotubes [8], 100 V is needed to drive the device due to its large square resistance ($1\text{ k}\Omega/\square$).

For the currently existing problems of low reliability, poor performance and high driving voltage, the high-performance thermoacoustic device must meet three conditions. First, the conductor should be thin enough with a low thermal capacity per unit area (HCPUA). Second, the conductor should prevent thermal leakage from the substrate (i.e. suspend). Third, the conductor area should be large enough to build a sufficient sound field. Graphene as a kind of two-dimensional layered material provides an opportunity for the development of thermoacoustic devices due to its ultralow HCPUA. After a lot of efforts, Ren's group has made some new achievements in graphene thermoacoustic devices. In particular, their graphene earphones and graphene throat have attracted widespread attention as their potential applications in solving the problem of human listening and speaking. Therefore, this chapter will detail the graphene sound sources, and explore the method of realization high performance devices.

2. Establishment of theoretical model

The physical image of thermoacoustic effect can be described as: when an alternating current signal is passing through the thin film, a film Joule heat is generated and quickly transferred to the surrounding air medium. Due to the periodic rise and fall of the surface temperature, a thin layer of air molecules on the film surface will continuously expand and contract to produce sound waves. **Figure 1a** shows the detailed physical process of the thermoacoustic device. The input AC signal (electric energy) is converted into Joule thermal fluctuation (thermal energy), and finally converted into sound waves (sound energy). Different from the principle of traditional acoustic devices, the conductive film itself does not vibrate itself but

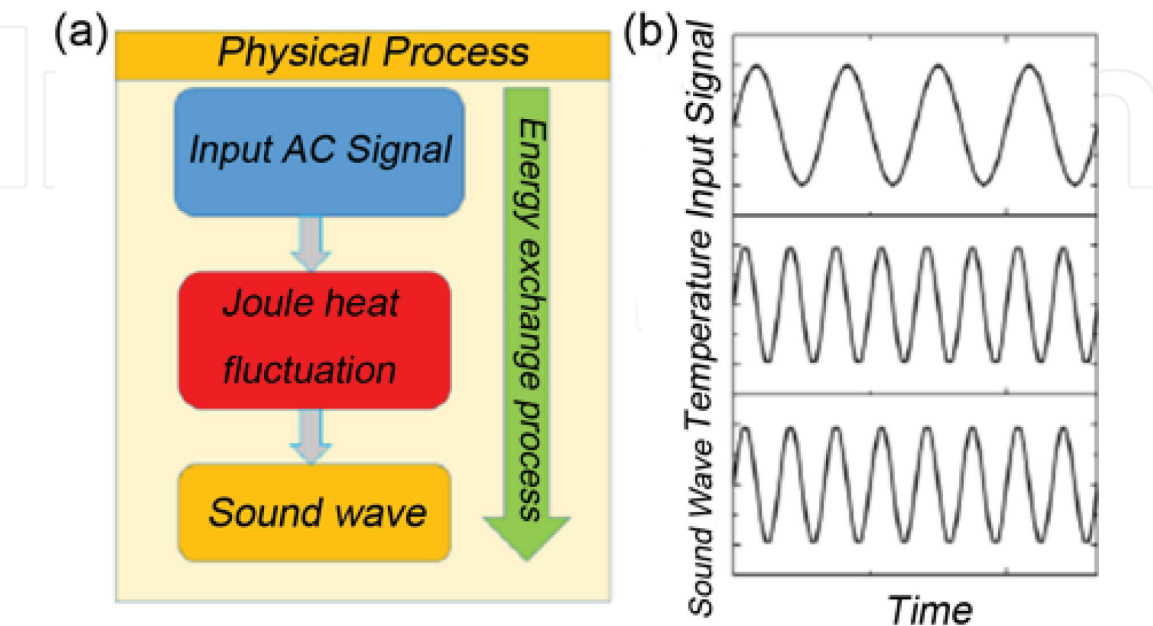


Figure 1. (a) Energy conversion process of thermoacoustic devices. (b) Theoretical waveforms during thermoacoustic effect [9].

makes the air vibrate by heating the air medium during the process of thermoacoustic effect. **Figure 1b** shows the theoretical waveforms corresponding to the three kinds of energy in the time domain. Assuming a sinusoidal signal is input, the Joule heat generated is squared with the electrical signal. Both positive half-cycle and negative half-cycle electrical signals can produce positive temperature fluctuations. Therefore, the frequency of temperature changes is twice the frequency of the input electrical signal, and the frequency of the sound waves is also doubled. This is an important feature that distinguishes the thermoacoustic effect from the traditional sound production.

In order to obtain high performance graphene sound source devices, it is necessary to carry out theoretical design to guide the experiment. Firstly, the theoretical model of thermoacoustic effect is established, and the sound pressure produced by graphene is predicted theoretically. The structure of graphene/substrate/back plate is proposed in **Figure 2**. The heat loss from the substrate should be taken into account due to the contact of graphene with the substrate. When the acoustic frequency is low, the heat flux can penetrate the substrate to reach the backplane, but when the sound frequency is high, the heat flux cannot reach the backplane. So it needs to be discussed in two frequency bands [9–11]:

when $f < \frac{\alpha_s}{4\pi L_s^2}$, the SP generated by graphene in the far field can be expressed as:

$$P_{rms} = \frac{\gamma - 1}{\sqrt{2} v_g} \frac{e_g}{M(e_s + a_c) + e_g} q_0 \tag{1}$$

when $f > \frac{\alpha_s}{4\pi L_s^2}$, the SP generated by graphene in the far field can be expressed as:

$$P_{rms} = \frac{\gamma - 1}{\sqrt{2} v_g} \frac{e_g}{(e_s + a_c) + e_g} q_0 \tag{2}$$

where f is frequency of sound; α_s and L_s are the thermal diffusivity and thickness of substrate, respectively; γ is the heat capacity ratio of gas; v_g is the sound velocity in gas; each layer has $e_i = \sqrt{K_i \rho_i C_{p,i}}$ is the thermal effusivity of material i . The

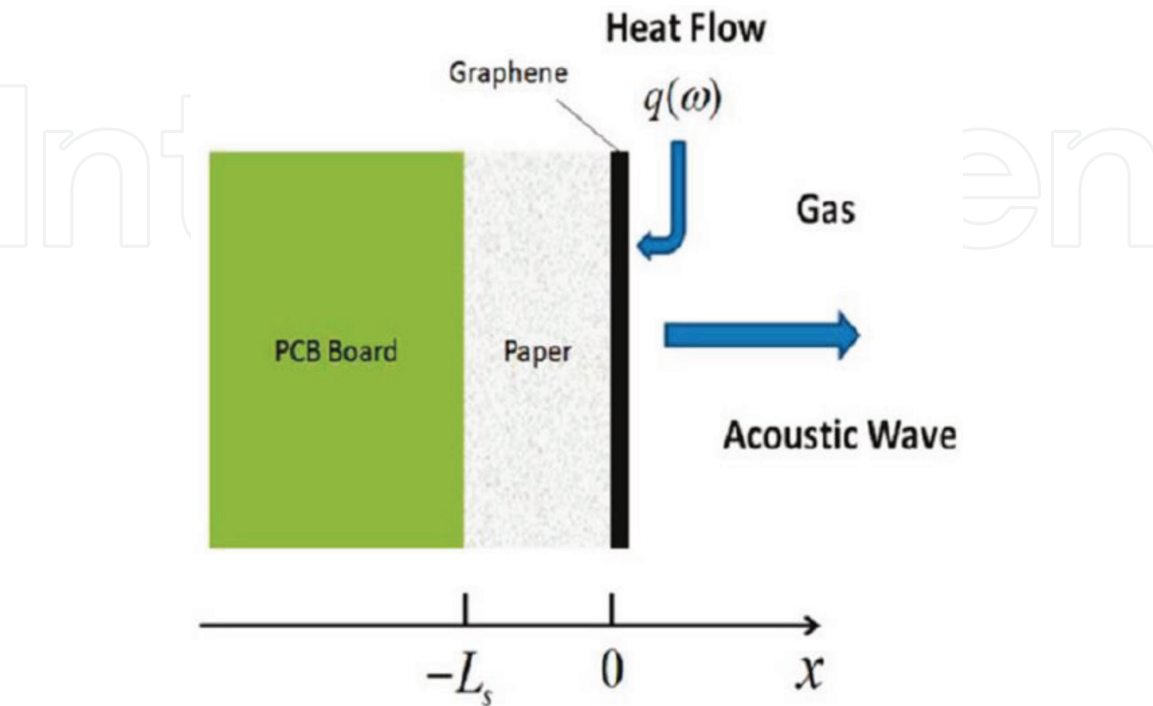


Figure 2.
Theoretical model of the graphene sound source [10].

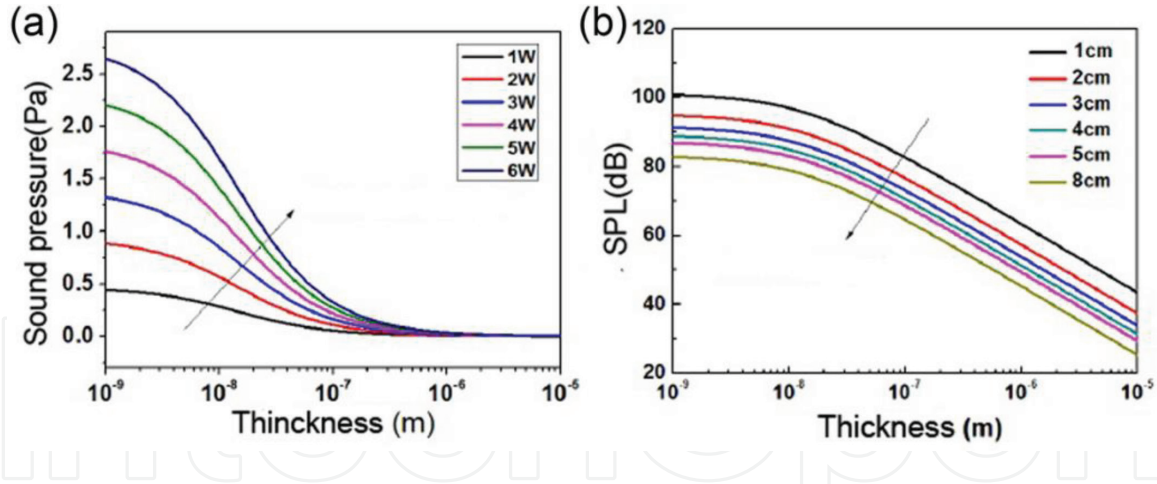


Figure 3.

(a) Theoretical relationship between SP and thickness of graphene under different input power conditions.

(b) Theoretical relationship between graphene SP and thickness under different test distance conditions [8].

subscript i represent gas (g), substrate (s), or backing layer (b), respectively. q_0 is the input power density; k_i , ρ_i and $C_{p,i}$ are the thermal conductivity, density and specific heat capacity of each layer of material, respectively; M is a frequency related factor. Under high frequency, $M \approx 1$, then the two equations are the same.

Based on the above theoretical formula, the relationship between the SP and thickness of graphene, input power and test distance can be calculated and analyzed. **Figure 3a** shows the theoretical waveform of SP. It can be seen that the corresponding SP value increases with the thickness of graphene decreasing, and the SP will increase as the input power increases at the same thickness. **Figure 3b** shows the theoretical relationship between SPL and graphene thickness at different test distances. At the same thickness, the SPL value will decrease as the test distance increases.

Then the sound field radiation of graphene sound source device is analyzed. The sound source device can be regarded as a point sound source in the far field, and the theoretical acoustic directivity $D(\theta, \varphi)$ can be expressed as [12]:

$$D(\theta, \varphi) = \text{sinc}\left(\frac{k_0 L_x}{2} \sin\theta \cos\varphi\right) \text{sinc}\left(\frac{k_0 L_y}{2} \sin\theta \sin\varphi\right) \quad (3)$$

where θ and φ are the parameters of the spherical coordinate system; $k_0 = 2\pi/\lambda_0$ is the wave number; Assuming that the sound source device is at the center of the sound field, L_x and L_y are the length and width of the sound source, respectively. **Figure 4** shows the directivity of the graphene point sound source at different sound frequencies. When the sound frequency is lower, the corresponding acoustic wave is longer, and the angle of sound field coverage is lower. With the increase of acoustic frequency, the acoustic wavelength decreases, and the sound field becomes more concentrated in the smaller angle perpendicular to the sample direction, that is, the directivity is enhanced.

Then, the sound field distribution of graphene device is analyzed, which includes near field and far field. Firstly, the distance of Rayleigh is defined as A/λ , where A and λ are the area and wavelength of graphene, respectively. The acoustic wave propagates in the form of plane wave when the test distance is smaller than Rayleigh distance in near field. However, when the measured distance is larger than Rayleigh distance, the acoustic wave propagates in the form of spherical waves in far field.

For $r < R_0$, the SP in near field can be expressed as:

$$P(\theta, \varphi) = \text{sinc}\left(\frac{k_0 L_x}{2} \sin\theta \cos\varphi\right) \text{sinc}\left(\frac{k_0 L_y}{2} \sin\theta \sin\varphi\right) \quad (4)$$

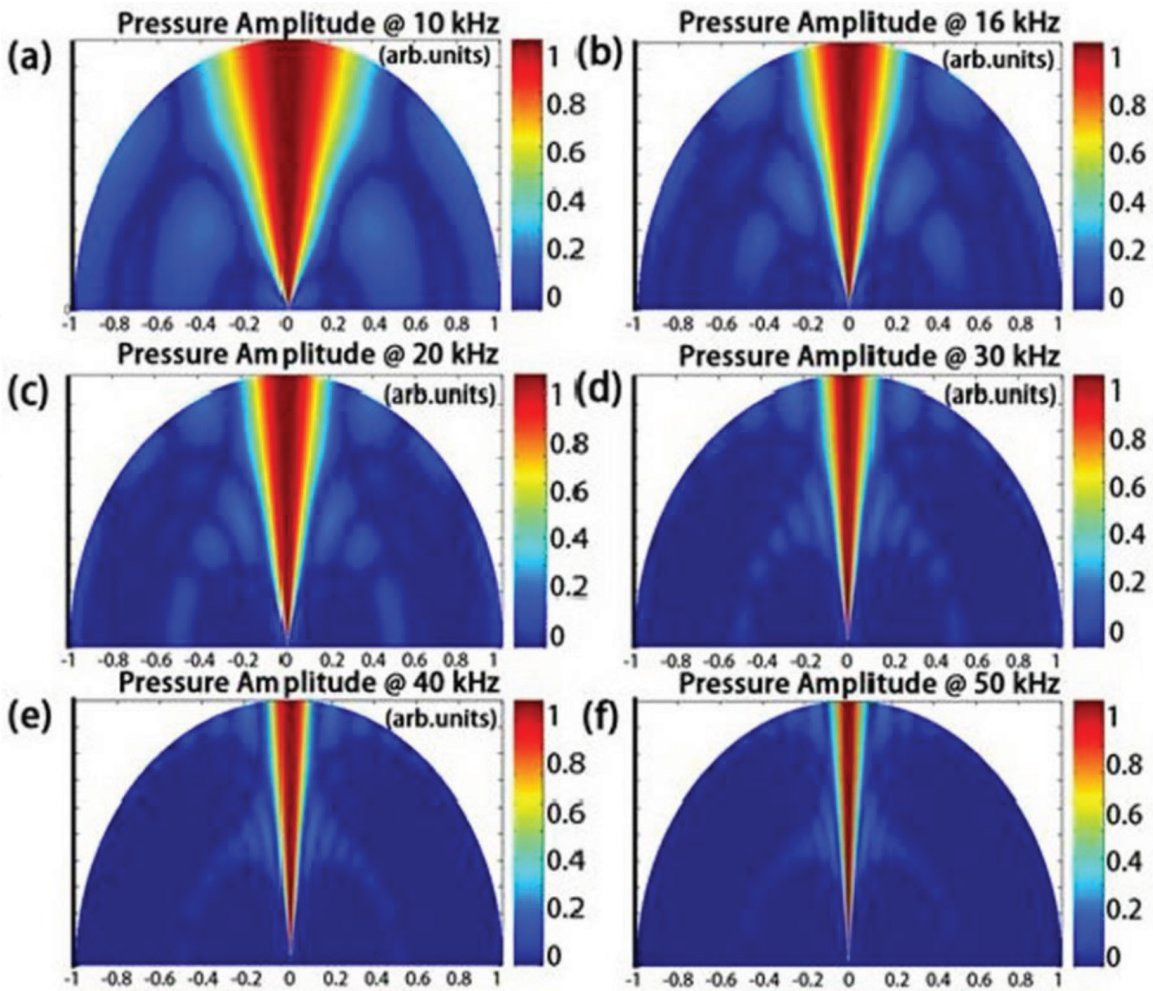


Figure 4. Directivity distribution of graphene sound source at different sound frequencies [9]. (a) 10 kHz, (b) 16 kHz, (c) 20 kHz, (d) 30 kHz, (e) 40 kHz, (f) 50 kHz.

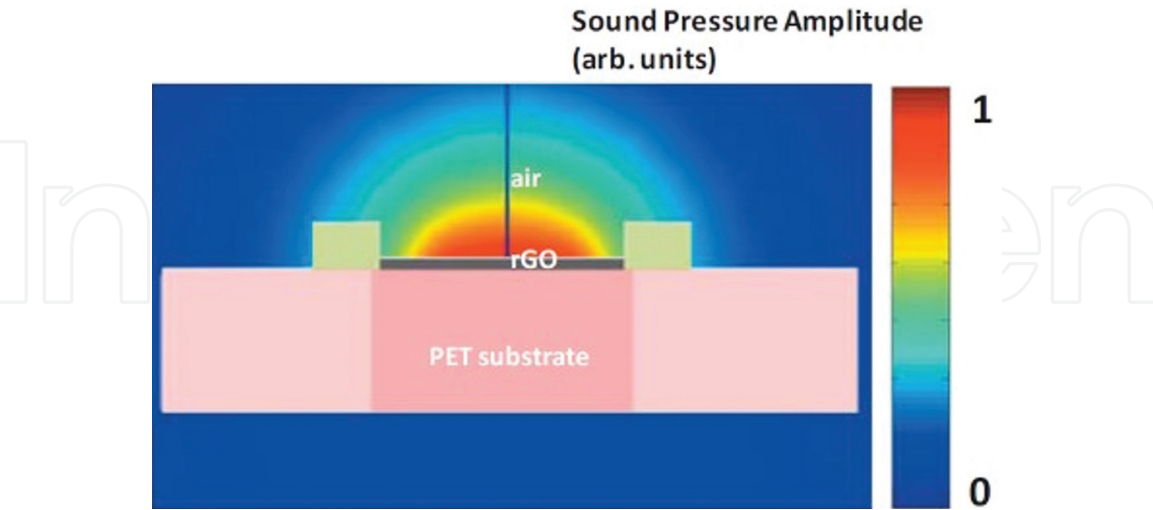


Figure 5. SP distribution of graphene sound source device obtained by finite element simulation [9].

For $r > R_0$, the SP in far field can be expressed as:

$$P(\theta, \varphi) = \frac{R_0}{r} \operatorname{sinc}\left(\frac{k_0 L_x}{2} \sin\theta \cos\varphi\right) \operatorname{sinc}\left(\frac{k_0 L_y}{2} \sin\theta \sin\varphi\right) \tag{5}$$

Based on the above two formulas, the theoretical distribution of graphene sound field can be simulated.

In order to fully consider the influence of the actual size of the device on the sound field distribution, the finite element software Comsol is used to simulate the sound field distribution. **Figure 5** shows the sound field distribution of graphene sound source devices simulated by finite element software. The simulation results show that the SP distribution on the surface of the device is stronger and the angle of sound coverage is wider. However, the sound coverage angle obtained by simulation is narrower when the point sound source approximation is used (**Figure 4**).

3. Graphene-on-paper sound source devices

The fabrication process of the multilayer graphene sound source device is introduced in **Figure 6**. Firstly, multilayer graphene was prepared on nickel foil by CVD method, the thickness of which was about 20 nm. Then, the graphene film of $1\text{ cm} \times 1\text{ cm}$ was transferred to filter paper. The transfer process was as follows: the FeCl_3 solution was used to etch graphene with nickel substrate. After nickel was etched, graphene was transferred to deionized water, and finally graphene was filled with porous filter paper. In the transfer process, filter paper with the pore size of $30\text{--}50\text{ }\mu\text{m}$ was used as substrate. Because the graphene film can be suspended on larger pores, which can effectively reduce heat loss to substrate and improve the efficiency of sound production. In order to test the sample acoustically, the sample was installed on the PCB board and the two electrodes were made. The Ag was used as electrode material of graphene sound source device. **Figure 6** shows the schematic diagram of a graphene-on-paper sound source device. When the sound frequency electric signal is applied to graphene device, the air near its surface can be heated, and then the periodicity of air vibration can induce sound waves.

Figure 7a shows the scanning electron microscope (SEM) image of the graphene. There are some ripples in graphene to get regular graphics. The oxygen plasma can be used to pattern graphene film. **Figure 7b** shows the image of the graphene film

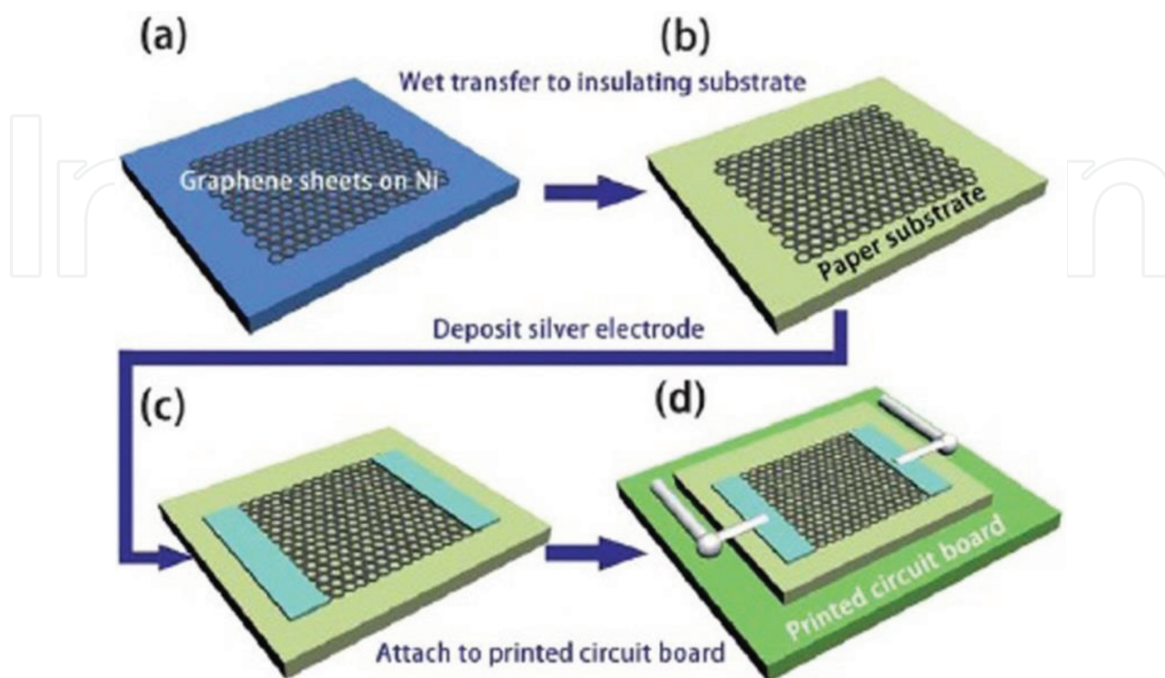


Figure 6.

A process for preparing a multilayer graphene sound source device: (a) growing a multilayer graphene on nickel; (b) transfer to filter paper by wet method; (c) prepare the Ag electrode at both ends of the graphene; (d) mount the device to the backplate and extract the signal [9].

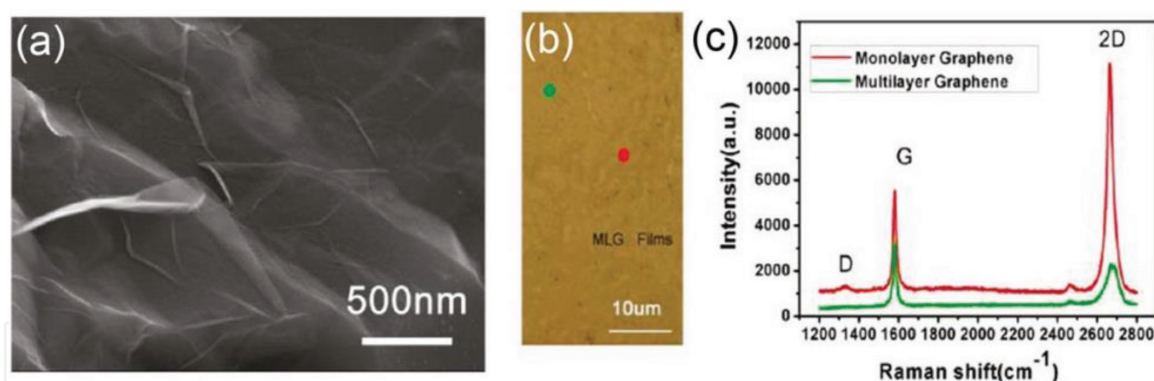


Figure 7. (a) SEM image of graphene. (b) An optical image of the graphene after oxygen plasma etching. (c) Raman spectrum in the range of $1200\text{--}2800\text{ cm}^{-1}$ of the graphene. The red line and green line correspond to the red and green part line in **Figure 7b**, respectively [9].

after oxygen plasma treatment. **Figure 7c** shows the Raman peak of the sample obtained from the corresponding colored spots in **Figure 7b**.

It can be seen that the two strong peaks locate at 1582 cm^{-1} and 2700 cm^{-1} , corresponding to G and 2D bands, respectively. The sample exhibits typical multilayered graphene characteristic with a strong G peak and a broad 2D peak (green line), while some spots exhibit monolayer graphene feature with a sharp G peak and a single higher 2D peak (red line). The small intensity of D-band observed at 1350 cm^{-1} indicates the low levels of defects and local-disorders in the deposited films.

Three paper-based graphene sound source devices are fabricated, named sample 1, sample 2 and sample 3, and their resistance are 32, 143, and $601\ \Omega$, respectively. The area of these devices is $1\text{ cm} \times 1\text{ cm}$, and the average thickness of three graphene sheet samples are about 100, 60, and 20 nm, respectively. The acoustics test platform is composed of a signal generator, a standard microphone and a dynamic frequency analyzer, as shown in **Figure 8a**. The signal generator drives the graphene sound source device to produce sound, and the sound wave is received by the standard microphone. Finally, the sound wave is analyzed by the dynamic frequency analyzer and the frequency is converted from time domain to frequency. The graphene sound source is directly tested by using a standard microphone (**Figure 8b**). The distance from the sound source to the microphone is 5 cm. The relationship between output SP and the input power is shown in **Figure 8c**. The result indicates that the SP increases linearly with increasing input power. **Figure 8d** shows the relationship between the SP and the test distance. For the graphene sound source devices, the Rayleigh distance can be calculated as $4.7 \times 10^{-3}\text{ m}$. The test distance of SP is ranging from 1 to $10 \times 10^{-2}\text{ m}$, which belongs to the far-field. The SP decreases with the increase of the test distance at 16 kHz sound frequency, indicating an inverse proportional to distance. This result is in agreement with the estimate of far-field. When the measure distance is 5 cm at 16 kHz sound frequency, the omnidirectional dispersion patterns can be achieved by testing the change of the SP with the receiving angle. The sound field directivity of multilayer graphene is shown in **Figure 8e**. The SP is mainly concentrated within the $\pm 30^\circ$ of the positive axis. After this angle, the SP is obviously attenuated. **Figure 8f** shows the relation between the output SPL and the frequency. The frequency is ranging from 3 to 50 kHz. The three curves are normalized with the same power density (1 W/cm^2) at different thickness of the graphene film. It can be seen that the 20 nm graphene film has the highest SPL value because of its lowest HCPUA. The 60 and 100 nm graphene rank second and third, respectively. It indicates that thinner graphene sheets can produce higher SPL. The sound frequency band can cover audible and ultrasound. Especially in ultrasound range 20–50 kHz, there exists flat frequency response.

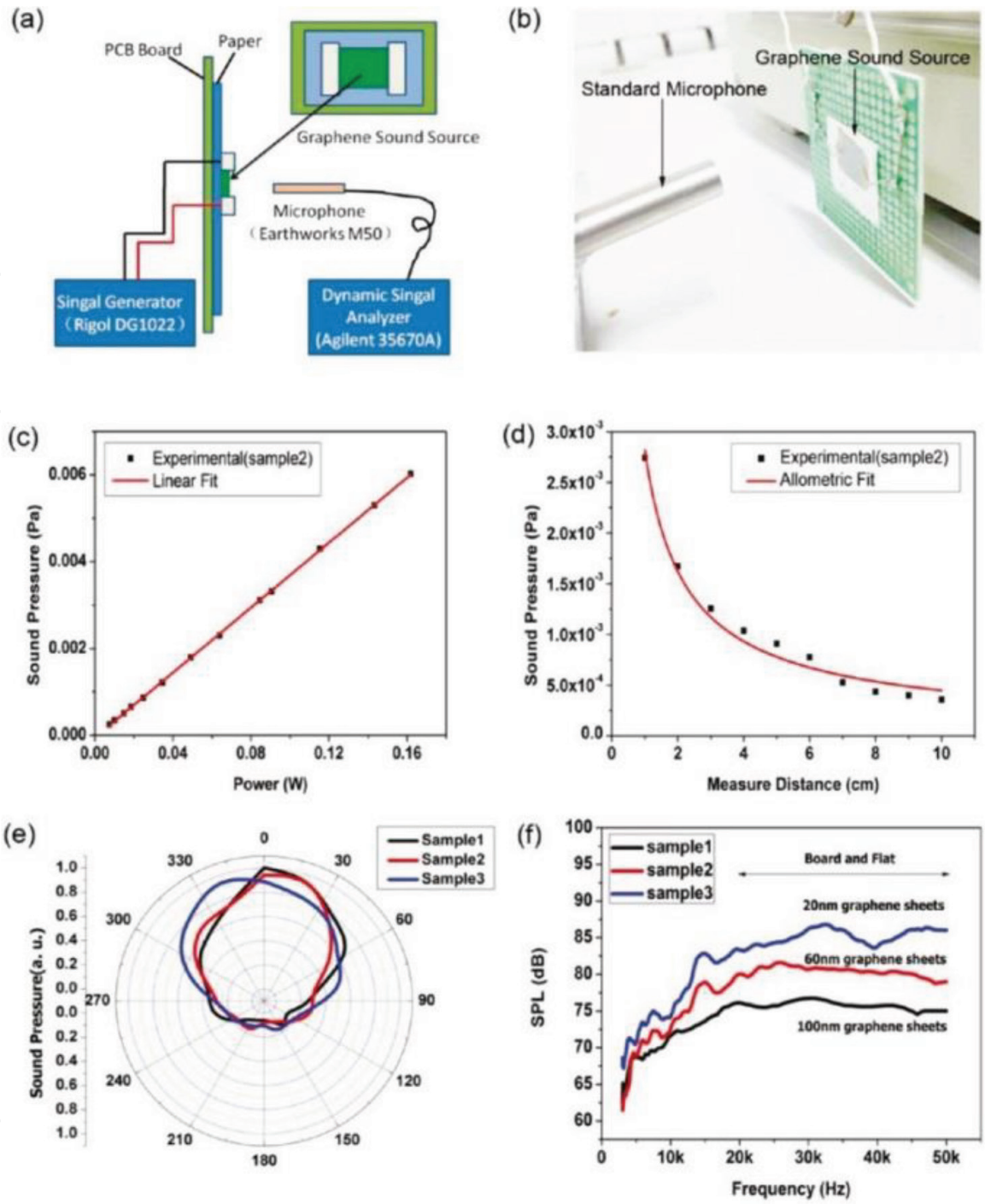


Figure 8. The acoustic test platform and test results of graphene sound source [10]. (a) Schematic diagram of test platform. (b) Onsite photo of the experimental setup. (c) The output SP from graphene versus the input power. (d) The plot of the output SP of graphene versus the measurement distance. (e) Directivity of the graphene sound source in far-field. (f) The output SPL versus the frequency. The three curves are normalized with the input power 1 W/cm².

The theoretical model has been introduced in the previous section. **Figure 9** shows the sound radiation of the graphene sound source in far-field. The on-axis direction has the largest sound intensity, the sound intensity decreases with the angle and the main intensity area focuses on axis ± 30 angles. Those results are agreed with the experimental directivity as shown in **Figure 8e**.

The physical scene of thermoacoustic effects is depicted in Arnold and Crandall's research results. When thermoacoustic device is working, alternating electrical signals generate joule heat through conductors. It would heat up the air near its surface and then the SP is generated by the changing of the air temperature. To verify this physical phenomenon through experiments, the advanced

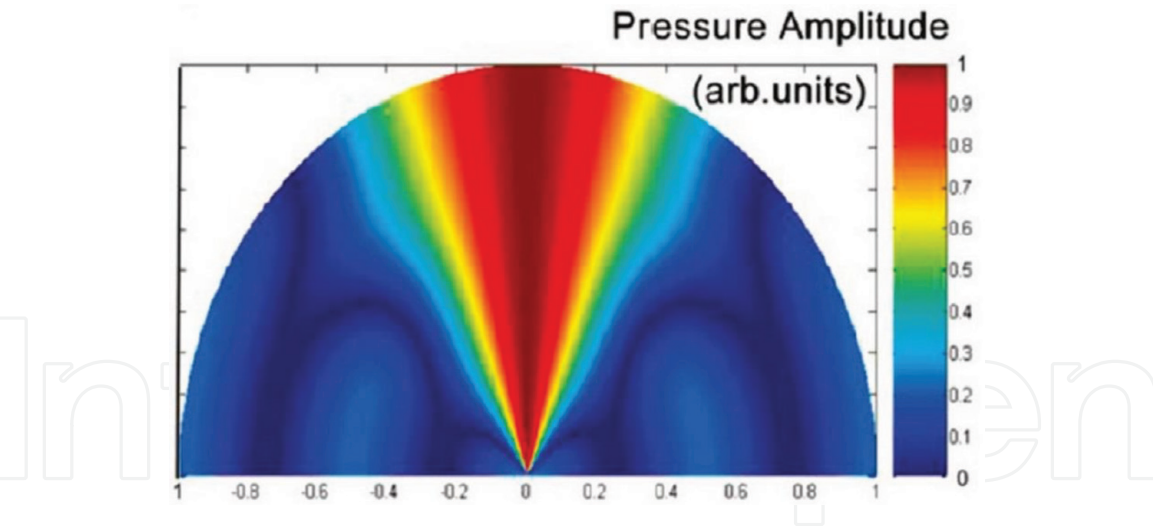


Figure 9.
Theoretical half-space directivity of the graphene sound source in far-field [10].

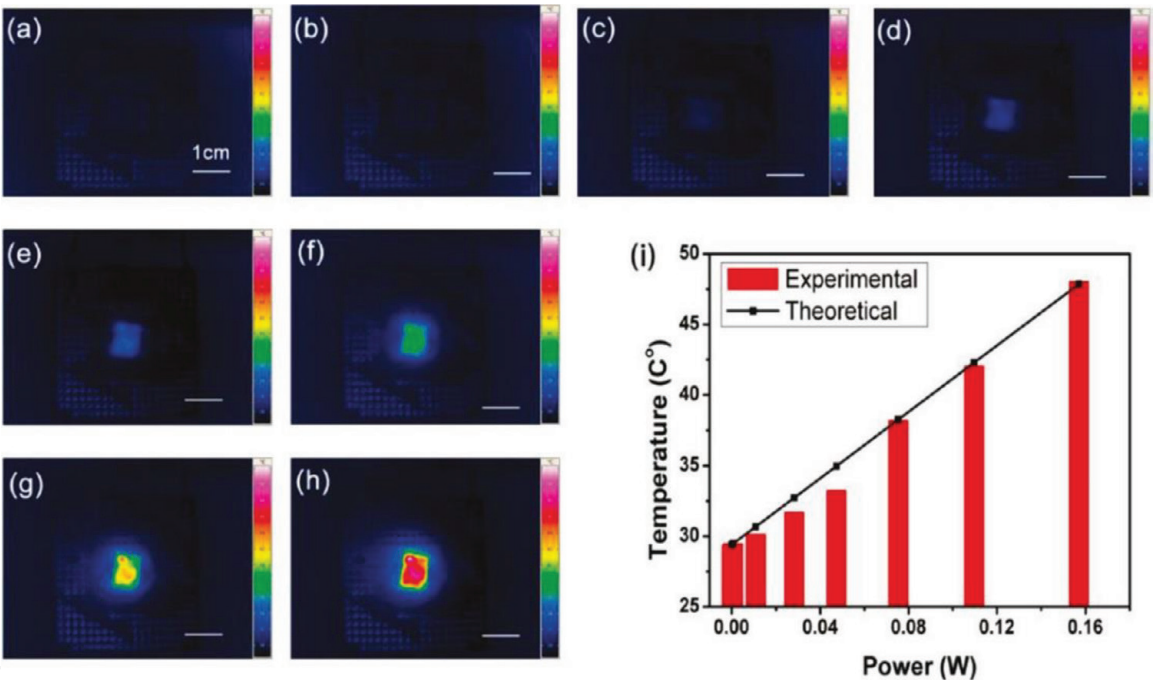


Figure 10.
Infrared thermal images and average surface temperature of graphene (sample 2) with different amplitude of input power [10] (a) no power is applied; (b) input power q_0 is 0.0007 W; (c) q_0 is 0.01 W; (d) q_0 is 0.03 W; (e) q_0 is 0.05 W; (f) q_0 is 0.08 W; (g) q_0 is 0.11 W; (h) q_0 is 0.16 W. (i) The average surface temperature of graphene versus the applied electric power. The experimental and theoretical results are shown. The SP is recorded at 16 kHz sound frequency and 5 cm measurement distance.

infrared thermal imaging instrument is used to investigate to the relations between the surface temperature distribution of graphene and the amplitude of input power. The input power q_0 is increasing from 0 to 0.16 W, the temperature distributions are collected in **Figure 10a–h**. The relationship between input power and graphene surface temperature is shown in **Figure 10i**. When the input power is 0 W, the surface temperature of the graphene is the same as that of room temperature. With the increase of input power, the surface temperature is gradually improved. The average surface temperature T of graphene can be expressed as [7]:

$$T = T_0 + \frac{q_0}{\sqrt{j\omega k_s C_{p,s}}} \tag{6}$$

where k_s and $C_{p,s}$ are the thermal conductivity and heat capacity of the paper substrate, respectively; ω is the angular frequency of sound. The average temperature is linearly related to the input power, and the theoretical curve is in good agreement with the experimental results. Combined with the test results of **Figure 8c**, the SP increases with the input power, which indicates that the Joule heating is related to the SP and the working mechanism is thermoacoustic effect.

4. Graphene earphones: entertainment for both humans and animals

Laser scribing can be used to prepare graphene due to its advantage of low cost, high speed and no transfer. The earphone based on laser scribed graphene (LSG) can cover audible range and ultrasonic range. Animal hearing is more sensitive to the sound of the ultrasound band than audible domain. Therefore, the graphene earphones can be applied not only to humans, but also to animals. This section will introduce laser direct writing to prepare graphene earphones. The advantage of fabricating graphene earphones by using the laser scribing technology is that the large scale array can be prepared without the mask. **Figure 11a** shows the preparation process of graphene earphones. The graphene oxide (GO) solution can be directly coated on PET substrates. Then the GO film can be reduced to graphene under 788 nm laser irradiation by using the DVD light engraving machine. It is noted that the preparation of the wafer-scale precise graphene earphones requires only 25 minutes by using laser scribing technology. **Figure 11b** shows the wafer-scale flexible graphene earphones on the PET substrate. The inset in **Figure 11b** shows the graphene earphones at 1 cm² dimensions. The SEM image of graphene sheets is shown in **Figure 11c**. Before the

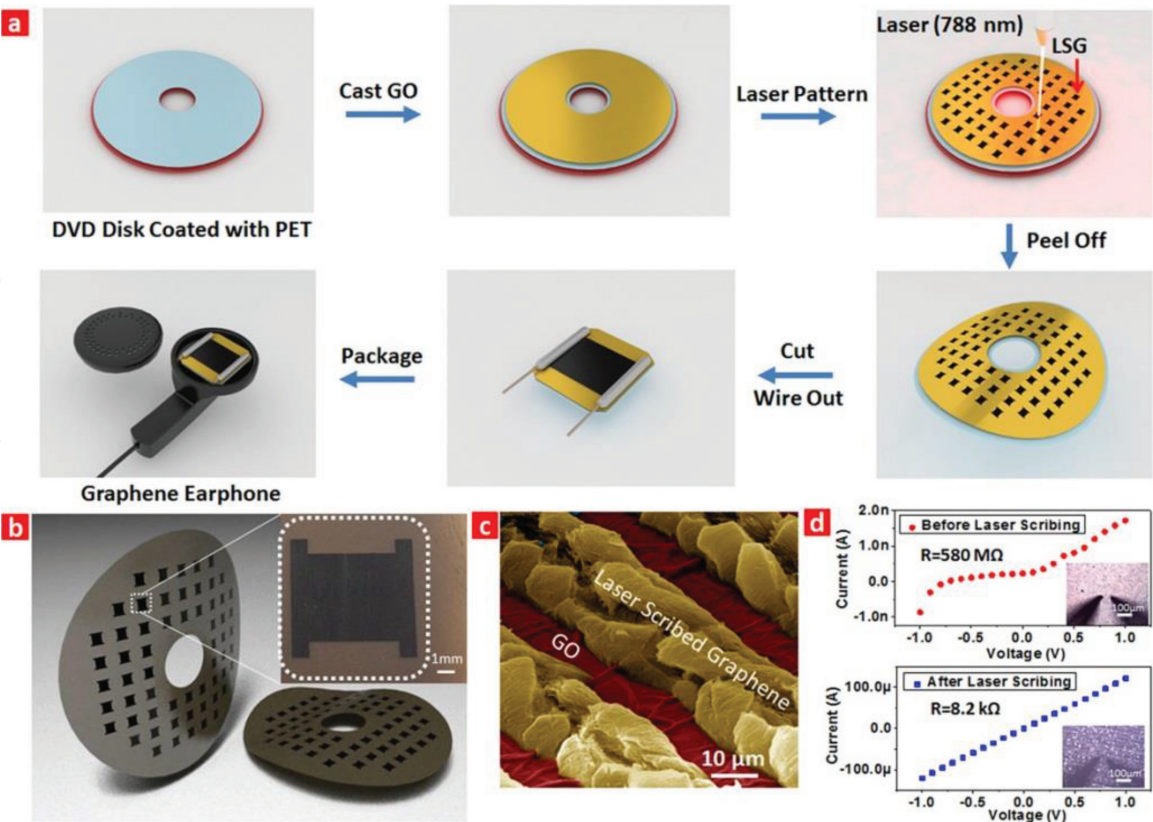


Figure 11. Laser scribing technology for flexible graphene earphone fabrication [13]. (a) Process flow of the graphene earphone fabrication; (b) wafer-scale flexible graphene earphones. The inset shows an optical microscope image of the LSG earphone; (c) SEM image of the LSG and GO in false color; (d) electrical properties before and after laser scribing.

laser scribing, the GO film is quite flat and dense. After the laser scribing, a graphene film of 10 μm thickness is obtained. It is noticed that there is an almost 10-fold thickness increase for the LSG compared to the original GO film. **Figure 11d** shows the I-V curves of the film before and after the laser scribing. The resistance of the GO film is 580 M Ω . However, when the GO film is reduced to the LSG, the small resistance can be obtained as 8.2 k Ω , which is an almost five orders of magnitude reduction.

Graphene sound source devices can be packaged into traditional earphones. After the laser scribing of the wafer-scale graphene patterns, these patterns could be cut into individual graphene earphones. **Figure 12a** shows the graphene earphone with an area of 10 \times 10 mm². Silver paste is applied on both sides of the graphene film to establish electrical input. The graphene earphones are finally connected to the electrical wiring of a commercial earphone casing using copper wires, as shown in **Figure 12b**. The structure of the graphene earphone is made up of the top cap, the graphene sheets, the Ag electrodes, the PET, and the bottom cap, as shown in **Figure 12c**. The packaged graphene earphones for human use is shown in **Figure 12d**. Compared with the traditional earphones, the distinctive feature of graphene device is significantly thinner than a voice coil. In order to obtain a sufficiently high SPL and equal-frequency playback sound, the periphery circuit is successfully designed. The schematic diagram of the circuit is shown in **Figure 13**. It is worth mentioning that the input sound frequency is doubled due to the thermoacoustic effect, and this needs to be compensated during actual testing, as described ahead. The drive circuit uses a USB port to apply power to the circuit for amplifying the AC signal and also to apply an up to 15 V DC bias to the graphene earphone. In this way, the graphene earphone can connect to a laptop for playing music.



Figure 12.
The demonstration of graphene earphone [13]. (a) Graphene earphone in hand. (b) View of the graphene earphone in a commercial earphone casing. (c) Exploded view of a packaged graphene earphone. (d) A pair of graphene earphones in its final packaged form.

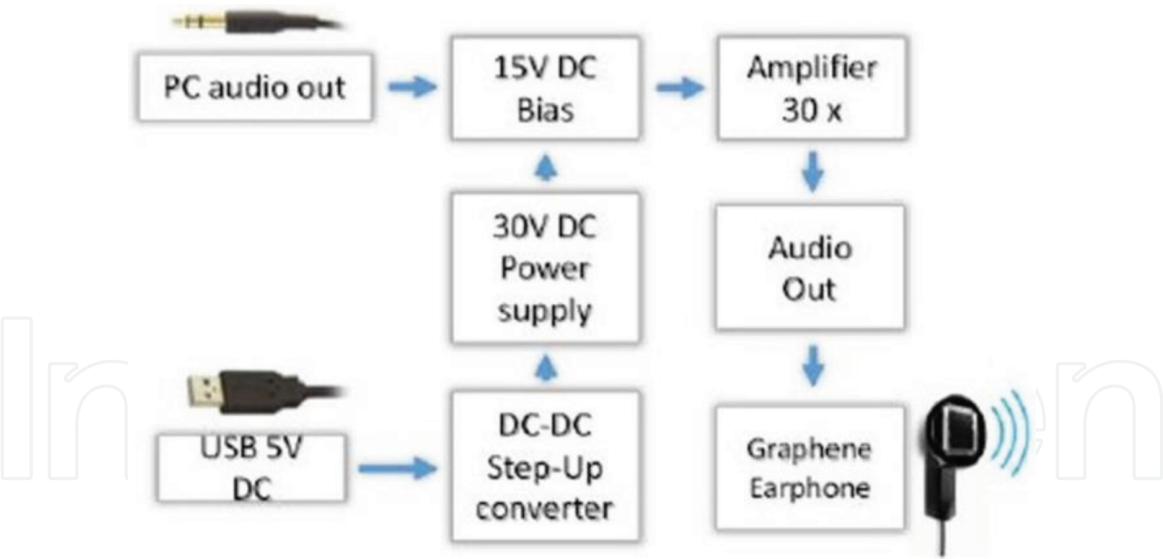


Figure 13.
Graphene earphone drive circuit structure diagram [9].

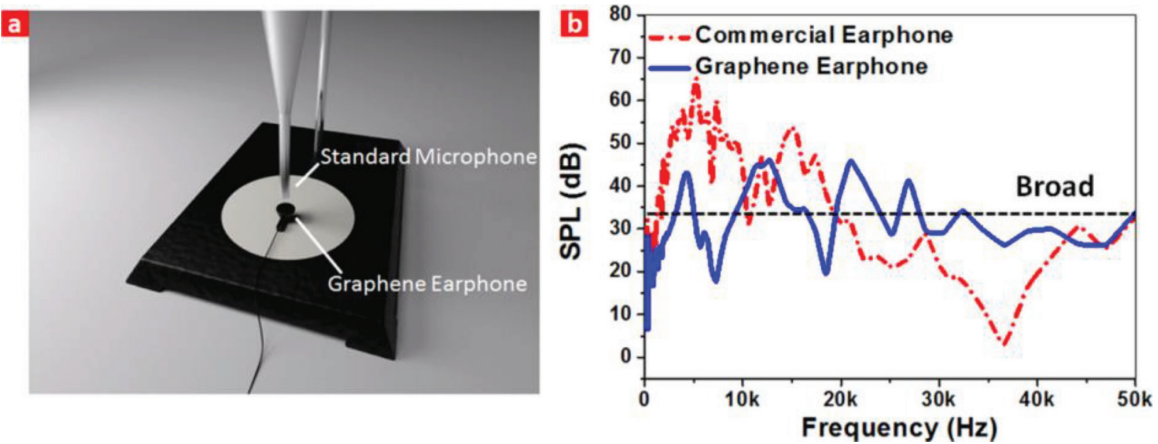


Figure 14.
Sound pressure and frequency characteristics of the graphene earphone [13]. (a) Experimental setup for the graphene earphone. (b) Sound pressure level (SPL) curves of a graphene earphone compared with a commercial earphone.

Figure 14a shows the graphene earphones acoustic test platform. **Figure 14b** shows the acoustic spectrum of the device. The graphene earphone is placed 1 cm away from the standard microphone. It can be seen that the graphene earphone has a flatter acoustic spectrum output than commercial earphone. Meanwhile, the sound intensity of the graphene earphone remains relatively stable. The graphene earphone has a fluctuation of 10 dB, which is much lower than the normal commercial earphone with the fluctuation of 30 dB. Especially, the spectrum can not only cover the 20 Hz to 20 kHz, but also cover the ultrasonic frequency band of 20–50 kHz. Animals are more sensitive to ultrasonic frequency than audible range, and graphene earphone has flat acoustic output in ultrasonic band. Therefore, graphene earphones can be used to train and control animal behaviors.

Finally, an application of the graphene earphone is demonstrated. The graphene earphone is fixed on the steel ring so that a dog can wear it, as shown in **Figure 15a** and **b**. The response test process is divided into the following sections. First, the dog needs to be trained so that it can recognize the “stand up” command when hearing the 35 kHz sound wave. The Chinese audio frequency of “stand up” was recorded first. Then, the audio was mixed with 35 kHz sine wave by computer software. The sampling frequency was 88.2 kHz, which was more than twice that of 35 kHz to ensure that the sampling was not distorted. The pure human voice was played to the

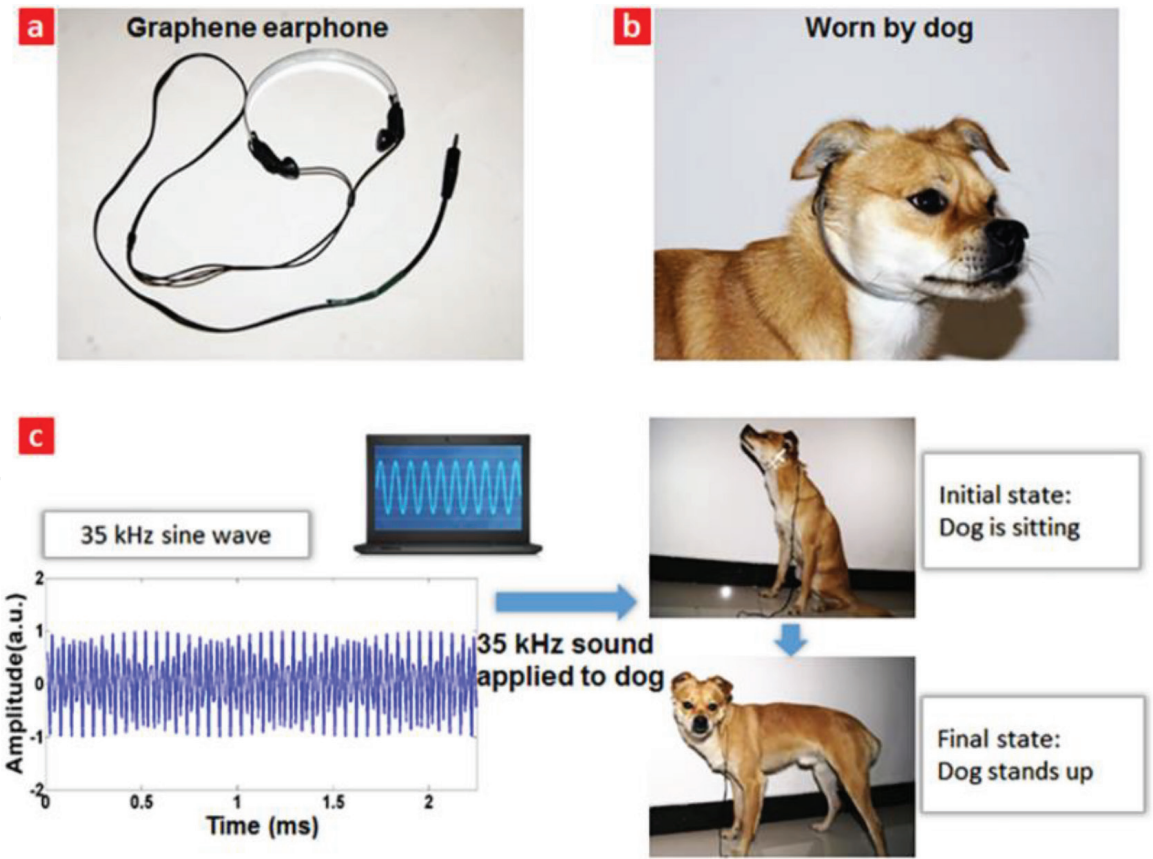


Figure 15. Animal responding to ultrasound signals through graphene earphone [13]. (a) Graphene earphone for dogs. (b) Subject wearing the graphene earphone. (c) Wearing a graphene earphone for the dog to establish a 35 kHz sound wave and a “stand up” command to reflect the training process. The dog is initially sitting down. After receiving a familiar 35 kHz signal, it stands up.

dog, and the dog will stand up, and then it will be mixed with 35 kHz sound waves. The dog will be given a food reward every time he stands up successfully. And then it went on to increase the proportion of 35 kHz sound waves, and to reduce the proportion of human voice. Until the final 35 kHz sound waves was 100%, the dog was able to stand up to prove that it was successful in establishing a 35 kHz sound wave to the dog and the “stand up” command. **Figure 15c** shows a demonstration of controlling dog behavior through graphene earphones. The initial state of the dog is sitting, and when the dog hears the 35 kHz sound from the graphene earphone, it will stand up, which indicates that the graphene earphone can control the dog’s behavior.

5. An intelligent artificial throat with sound-sensing ability based on laser-induced graphene

The graphene sound source device based on thermoacoustic effect is introduced. Based on its piezoresistive effect, graphene can also be used for throat detection, which can be used as a good sound receiver. Therefore, based on thermoacoustic effect and piezoresistive effect, graphene is expected to realize transceiver integration.

At the present stage, devices with integrated sound and transceiver function are usually called ultrasonic transducers, which can only work in the ultrasonic frequency band or under water [14]. At the same time, these substrates are hard, not flexible and biocompatible, and not suitable for wearable applications. Therefore, studying the audible frequency band, the sound-flexible device with good flexibility and biocompatibility is of great significance.

Graphene force acoustic devices are mainly faced with two problems: (1) Sound receiving device based on graphene piezoresistive effect cannot be used as sound emitting device because these devices are wrapped in a polymer and the heat cannot be released into the air [15]. Or the device has a higher resistance, resulting in poor thermoacoustic effects [16]. (2) Sounding devices based on the thermoacoustic effect of graphene are also not suitable as sound receivers. Because these devices are fabricated by using single layer or few layer graphene [17]. These kinds of graphenes are easily broken, which cause the devices damage. Graphene devices based on conventional processes and methods are difficult to simultaneously receive sound and emit sound using thermoacoustic effects and piezoresistive effects. Therefore, it is necessary to explore the realization of graphene transceiver sound integration based on new materials and new technology.

The method of laser scribed graphene (LSG) is described above. However, graphene reduced by this method cannot be simultaneously transmitted and received sound due to packaging reasons. In 2014, Lin et al. proposed a method for preparing porous structure graphene by laser reduction of polyamide material (PI) [18]. This method can be completed in a single step process without the need to drop coating GO, and the prepared graphene has a porous structure and a good piezoresistive effect. Because graphene materials have good thermal properties, they can make sound based on thermoacoustic effect. Therefore, the porous graphene based on laser reduction can be used to fabricate the flexible force acoustic device to realize sound transmission and reception integration.

This chapter introduces the process of preparing porous graphene by 450 nm wavelength laser. The porous graphene has the ability to integrate sound transmission and reception based on thermoacoustic effect and piezoresistive effect. Hence, a new intelligent artificial throat was prepared based on porous graphene. This device can be attached to the throat to sense the vibration mode of the throat of the deaf mute, and emit a preset sound when a specific throat vibration mode is detected. Therefore, the artificial throat can assist the deaf and mute to achieve sound, which will have potential application in biomedical, acoustic and other fields.

Laser direct writing technology promotes the fast growth of porous, and a low-cost and portable laser platform is chosen. **Figure 16a** is a schematic diagram of a laser processing platform. The 450 nm laser can directly reduce the yellow PI to the porous graphene. Then, the artificial throat based on the porous graphene has been integrated to achieve the functions of emitting and detecting sounds, as shown in **Figure 16b**. **Figure 16c** shows the working mechanism of the artificial throat. When AC voltage is applied to the device, the periodic joule heat will cause air to expand, thus producing sound waves. When a low bias voltage is applied to the device, the vibration of the throat leads to the change of the resistance of the device, resulting in current fluctuations. Therefore, this device can act as both sound sources and detectors. A coughs, buzzing or screams can cause throats to vibrate, which can be detected by LSG artificial throats, and then LSG artificial throats can produce controllable sounds. Therefore, LSG artificial throat can achieve the conversion from meaningless sound to controllable and pre-designed sound. **Figure 16d** shows the image of LSG at laser power ranging from 20 to 350 mW. It can be seen that there is no obvious LSG at the bottom when the power is 20 mW. The second black part and the fourth black part from the bottom, which are produced at the power of 125 and 290 mW, respectively, are chosen to show the SEM image, as shown in **Figure 16e–j**. It can be seen that regular ridge lines are formed from top to bottom along the laser scanning trajectory. The line width is approximately 100 μm , which is similar to the focused spot size of the laser. As the laser power increases, the morphological differences are significant. A polygonal porous carbon film appears at the power of 125 mW. However, when the power is 290 mW, more porous irregular structures can be produced. This is mainly

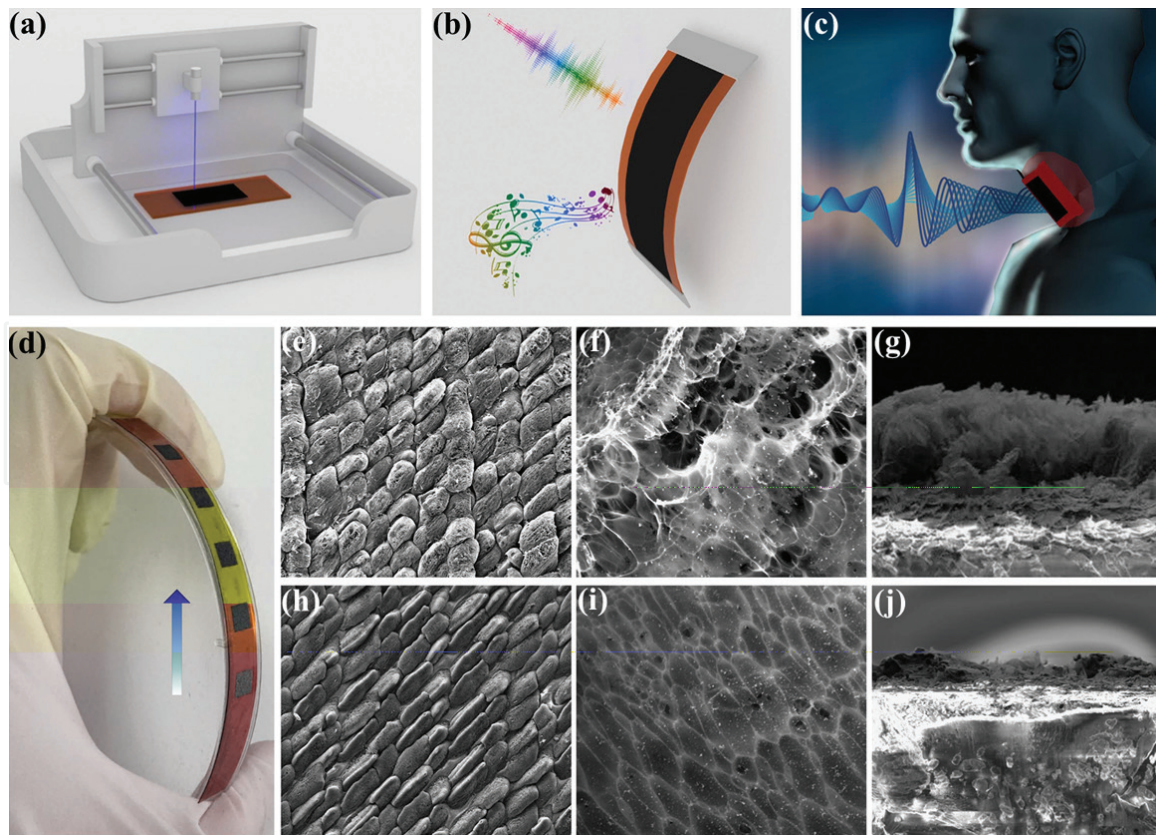


Figure 16. (a) One-step fabrication process of LSG. (b) LSG has the ability of emitting and detecting sound in one device. (c) The artificial throat can detect the movement of throat and generate controllable sound, respectively. (d) Si_x LSG samples produced by 450 nm laser with different power ranging from 20 to 350 mW. (e) The morphology of LSG sample produced at 290 mW under scanning electron microscopy, scale bar, 150 μm . (f) The morphology of LSG sample produced at 290 mW under high magnification, scale bar, 5 μm . (g) Cross-sectional view of LSG sample produced at 290 mW, scale bar, 12.5 μm . (h) The morphology of LSG sample produced at 125 mW under scanning electron microscopy, Scale bar, 150 μm . (i) The morphology of LSG sample produced at 125 mW under high magnification, Scale bar, 5 μm . (j) Cross-sectional view of LSG sample produced at 125 mW, scale bar, 12.5 μm [19].

because the high power will lead to a sharp rise of the PI local temperature, thus breaking the C–O, C=O and N–C bonds, and causing the venting of some carbonaceous and nitric gases. Therefore, the porous structure of sample is formed due to the production and discharge of gases.

Four samples of LSG artificial throats are produced at different laser powers. The area of the LSG is around $1 \times 2 \text{ cm}^2$. The laser powers are 125, 200, 290 and 350 mW, respectively. The average thickness of LSG is about 8, 22, 38 and 60 μm , corresponding to the laser power. **Figure 17a** is a test diagram of the device. The distance between the sample and standard microphone is 2.5 cm. **Figure 17b** shows the relationship of the LSG (produced under 125 mW) between input power and SP. The result indicates that the SP increases linearly with increasing input power, and a higher SP can be obtained at 20 kHz. **Figure 17c** shows the spectrum response of the LSG produced by different power. The input power is normalized to 1 W. It can be observed that the SPL gradually decreases with the increase of power. **Figure 17d** shows the comparison of theoretical curve and the experimental results. The experimental analysis matches well with the theory model. **Figure 17e** shows the experimental data and theoretical curve as a function of the thickness of the LSG under the frequency of 10 and 20 kHz. The SP is inversely proportional to the thickness of the sounding unit and the theoretical curve matches well with the experimental results. **Figure 17f** shows the stability of LSG. It can be seen that there are no signs of degradation or changes of SPL in the device performance in 3 hours.

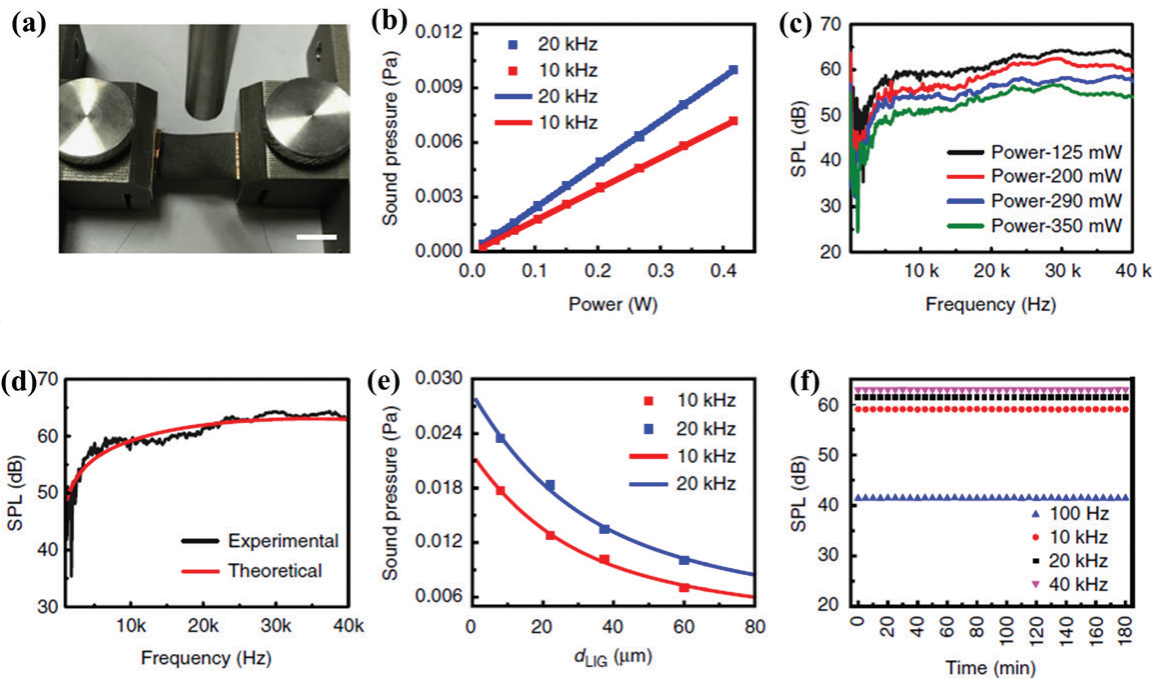


Figure 17. (a) The LSG is clamped under a commercial microphone to test the performance of emitting sound, scale bar, 1 cm. (b) The plot of the SP versus the input power at 10 and 20 kHz. (c) The output SPL versus the frequency of LSG generated by the laser with different power. (d) The SPL versus the frequency showing that the model agrees well with experimental results. (e) The plot of the SP versus the thickness of LSG at 10 and 20 kHz. (f) The stability of output SPL over time [19].

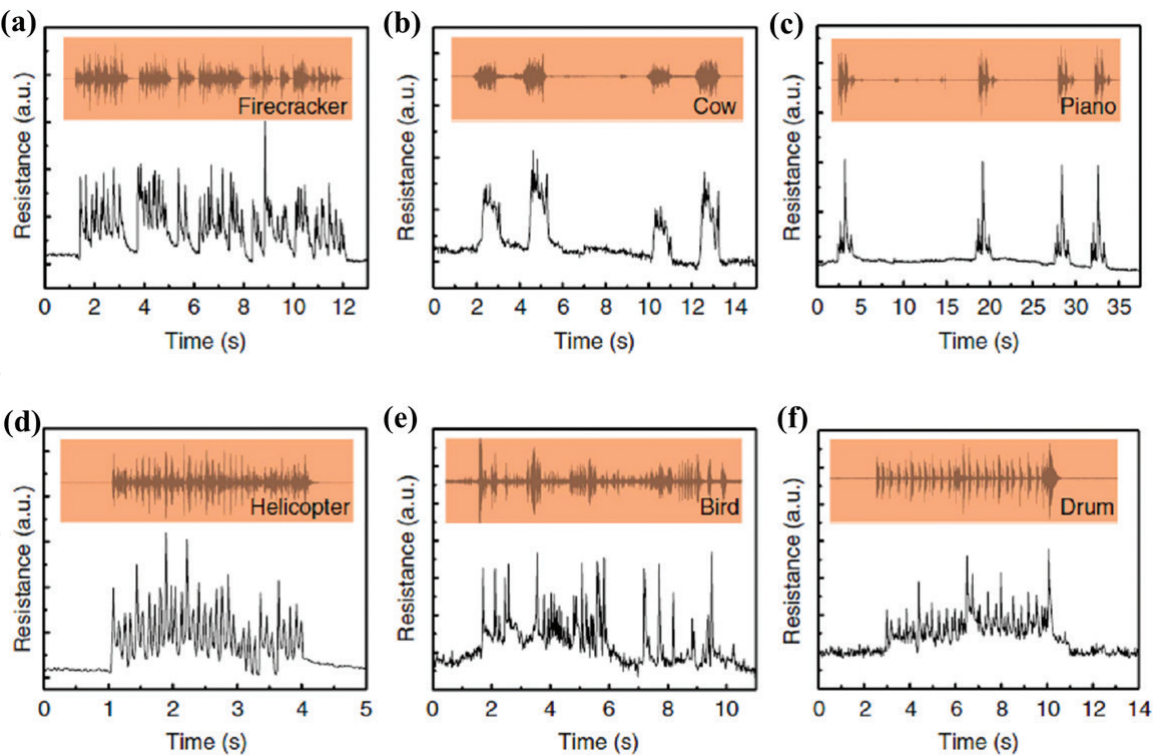


Figure 18. Responses towards different audios from a loudspeaker [19]. The LSG is placed 3 cm away from the loudspeaker. The orange insets above indicate the sound wave profiles of the original audios. Relative resistance changes show almost synchronous response to profiles of the original audios when the loudspeaker plays the audio of (a) firecrackers, (b) a cow, (c) a piano, (d) a helicopter, (e) a bird and (f) a drum.

Except for emitting sound, the LSG artificial throat also has excellent responses when detecting sound. The 25 μm -thick PI can be chosen to produce the LSG due to obvious resistance change. The sample is fixed and the loudspeaker is placed 3 cm

away from the artificial throat. The six kinds of audios including firecracker, cow, piano, helicopter, bird and drum are performed. **Figure 18** shows the resistance response of the device at six kinds of audios. Although the sampling frequency of this artificial throat is 100 Hz, which is far lower than the frequency of sound, it can be still noticed that the responses of the transducer are well synchronous to these original audio signals. Especially, the characteristic peaks are retained and reflected with high fidelity. Besides, the volume of loudspeaker has a great effect on the amplitude of the signal.

After identifying some kinds of audio clearly, LSG artificial throat is used to detect the vibration of throat cords. As shown in **Figure 19a**, the tester performs coughing, snoring and screaming twice in succession, and then the tester swallows and nods twice. After two consecutive tests, the test results are reproducible. In addition, swallowing and nodding can also cause muscle movement, which can also lead to changes in resistance. Fortunately, the waveforms of these muscle movements also have identifiable features. Different movement has its unique characteristic waveform as shown in **Figure 19a**, thus, the useful waveforms can be gotten by relying on the pattern recognition and machine learning. Interference from other activities can be identified and eliminated by multiple trainings in advance. Then, the tester makes the hums with four different tones as shown in **Figure 19b**,

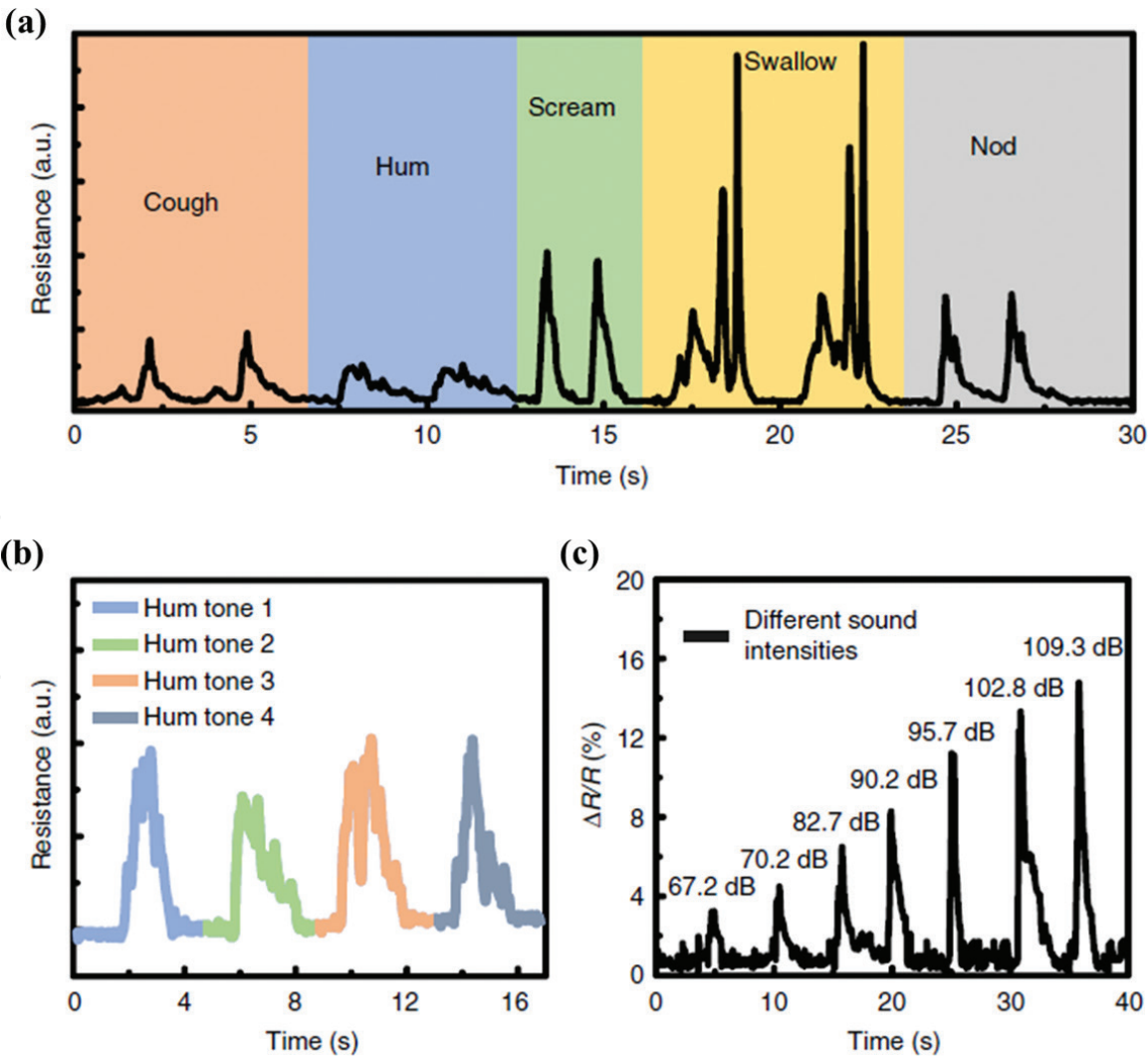


Figure 19. Responses towards different kinds of throat vibrations. (a) The LSG's resistance changes towards the throat vibrations of the tester who makes two successive coughs, hums, screams, swallowing and nods. (b) The LSG's resistance change caused by four different kinds of hum tones and the hum tone 2 is same with the hum in (a). (c) The relative resistance change of LSG increases with the increase of the sound intensities of the hum [19].

it can be seen that different tones have different responses, increasing the diversity of dumb people's "language". Especially, the hum tone 2 is same with the hum in **Figure 19a**. Furthermore, as shown in **Figure 19c**, the resistance increases as the sound intensity increases, which is due to the increase in mechanical vibration of the throat.

6. Conclusion

Thermoacoustic device for the current low reliability, high performance and poor driving voltage problem, Ren's group successfully proposed and implemented graphene thermoacoustic devices with high performance, high reliability and low driving voltage. Besides, these devices have the advantages of low driving voltage, soft, transparent, thin thickness and wide band sound output, especially the extremely flat sound output in the ultrasonic frequency band. Exploring the application of graphene in the field of acoustics is the first time in the world and obtains the following three research results:

1. A multilayer graphene sound source device is proposed and realized. The sound output performance from 1 to 50 kHz is obtained. It is observed that there is a flat sound spectrum in the range of 20–50 kHz. The performance of multilayer graphene sound source device with different thickness is compared. It was found that graphene with thinner thickness had a higher SPL value.
2. A low cost graphene earphones at wafer level are realized by laser scribing. Graphene earphone has a wider and flatter acoustic spectrum output than commercial earphones. In addition, graphene earphone achieves control of animal behavior.
3. A wearable artificial throat that is manufactured in one step based on LSG has been implemented. The LSG device achieves the functional integration of emitting and detecting sound due to its excellent thermoacoustic and piezoresistive properties. The LSG artificial throat has a relatively broad frequency spectrum because of resonance-free oscillations of the sound sources. Besides, as a sound detector, the LSG artificial throat can capture the mechanical vibration of throat cords with a fine repetition.

Acknowledgements

This work was supported by the National Key R&D Program (2016YFA0200400), National Natural Science Foundation (61434001, 61574083, 61874065, 51861145202), and National Basic Research Program (2015CB352101) of China. He Tian thanks for the support from Young Elite Scientists Sponsorship Program by CAST (2018QNRC001). The authors are also thankful for the support of the Research Fund from Beijing Innovation Center for Future Chip, Beijing Natural Science Foundation (4184091), and Shenzhen Science and Technology Program (JCYJ20150831192224146).

IntechOpen

Author details

He Tian^{1,2*†}, Guang-Yang Gou^{1,2†}, Fan Wu^{1,2}, Lu-Qi Tao^{1,2}, Yi Yang^{1,2*}
and Tian-Ling Ren^{1,2*}

1 Institute of Microelectronics, Tsinghua University, Beijing, China

2 Beijing National Research Center for Information Science and Technology
(BNRist), Tsinghua University, Beijing, China

*Address all correspondence to: tianhe88@tsinghua.edu.cn; yiyang@tsinghua.edu.cn
and rentl@tsinghua.edu.cn;

† These authors contributed equally to this work.

IntechOpen

© 2019 The Author(s). Licensee IntechOpen. This chapter is distributed under the terms of the Creative Commons Attribution License (<http://creativecommons.org/licenses/by/3.0>), which permits unrestricted use, distribution, and reproduction in any medium, provided the original work is properly cited. 

References

- [1] Novoselov KS, Geim AK, Morozov SV, et al. Electric field effect in atomically thin carbon films. *Science*. 2004;**306**:666-669
- [2] Ho KI, Boutchich M, Su CY, et al. A self-aligned high-mobility graphene transistor: Decoupling the channel with fluorographene to reduce scattering. *Advanced Materials*. 2015;**27**:6519-6525
- [3] Li D, Chen M, Zong Q, et al. Floating-gate manipulated graphene-black phosphorus heterojunction for nonvolatile ambipolar schottky junction memories, memory inverter circuits, and logic rectifiers. *Nano Letters*. 2017;**17**:6353-6359
- [4] Sarker BK, Cazalas E, Chung TF, et al. Position-dependent and millimetre-range photodetection in phototransistors with micrometre-scale graphene on SiC. *Nature Nanotechnology*. 2017;**12**:668-674
- [5] SMM Z, Holt M, Sadeghi MM, et al. 3D integrated monolayer graphene-Si CMOS RF gas sensor platform. *npj 2D Materials and Applications*. 2017;**1**:36
- [6] Arnold HD, Crandall IB. The thermophone as a precision source of sound. *Physical Review*. 1917;**10**:22
- [7] Shinoda H, Nakajima T, Ueno K, et al. Thermally induced ultrasonic emission from porous silicon. *Nature*. 1999;**400**:853-855
- [8] Xiao L, Chen Z, Feng C, et al. Flexible, stretchable, transparent carbon nanotube thin film loudspeakers. *Nano Letters*. 2008;**8**:4539-4545
- [9] Tian H. *Graphene-Based Novel Micro/Nano Devices*. Beijing: Tsinghua University; 2015
- [10] Tian H, Ren TL, Xie D, et al. Graphene-on-paper sound source devices. *ACS Nano*. 2011;**5**:4878-4885
- [11] Blackstock DT. *Fundamentals of Physical Acoustics*. Vol. 465. New York: John Wiley and Sons, Ltd; 2000. p. 440
- [12] Vesterinen V, Niskanen AO, Hassel J, Helisto P. Fundamental efficiency of nanothermophones: Modeling and experiments. *Nano Letters*. 2010;**10**:5020-5024
- [13] Tian H, Li C, Mohammad MA, et al. Graphene earphones: Entertainment for both humans and animals. *ACS Nano*. 2014;**8**:5883-5890
- [14] Meeks SW, Timme RW. Rare earth iron magnetostrictive underwater sound transducer. *The Journal of the Acoustical Society of America*. 1977;**62**:1158-1164
- [15] Park JJ, Hyun WJ, Mun SC, et al. Highly stretchable and wearable graphene strain sensors with controllable sensitivity for human motion monitoring. *ACS Applied Materials & Interfaces*. 2015;**7**:6317-6324
- [16] Cheng Y, Wang R, Sun J, et al. A stretchable and highly sensitive graphene-based fiber for sensing tensile strain, bending, and torsion. *Advanced Materials*. 2015;**27**:7365-7371
- [17] Tian H, Xie D, Yang Y, et al. Single-layer graphene sound-emitting devices: Experiments and modeling. *Nanoscale*. 2012;**4**:2272-2277
- [18] Lin J, Peng Z, Liu Y, et al. Laser-induced porous graphene films from commercial polymers. *Nature Communications*. 2014;**5**:5714
- [19] Tao LQ, Tian H, Liu Y, et al. An intelligent artificial throat with sound-sensing ability based on laser induced graphene. *Nature Communications*. 2017;**8**:14579